Magnetotransport of Dirac fermions on the surface of a topological insulator

S. Mondal,[1] D. Sen,[2] K. Sengupta,[1] and R. Shankar[3]
[1]*Theoretical Physics Division, Indian Association for the Cultivation of Sciences, Kolkata 700 032, India*
[2]*Center for High Energy Physics, Indian Institute of Science, Bangalore 560 012, India*
[3]*The Institute of Mathematical Sciences, C.I.T. Campus, Chennai 600 113, India*
(Received 2 April 2010; revised manuscript received 3 July 2010; published 23 July 2010)

We study the properties of Dirac fermions on the surface of a topological insulator in the presence of crossed electric and magnetic fields. We provide an exact solution to this problem and demonstrate that, in contrast to their counterparts in graphene, these Dirac fermions allow relative tuning of the orbital and Zeeman effects of an applied magnetic field by a crossed electric field along the surface. We also elaborate and extend our earlier results on normal-metal-magnetic film-normal metal (NMN) and normal-metal-barrier-magnetic film (NBM) junctions of topological insulators [S. Mondal, D. Sen, K. Sengupta, and R. Shankar, Phys. Rev. Lett. **104**, 046403 (2010)]. For NMN junctions, we show that for Dirac fermions with Fermi velocity v_F, the transport can be controlled using the exchange field $\mathcal{J}$ of a ferromagnetic film over a region of width d. The conductance of such a junction changes from oscillatory to a monotonically decreasing function of d beyond a critical $\mathcal{J}$ which leads to the possible realization of magnetic switches using these junctions. For NBM junctions with a potential barrier of width d and potential V_0, we find that beyond a critical $\mathcal{J}$, the criteria of conductance maxima changes from $\chi=eV_0d/\hbar v_F=n\pi$ to $\chi=(n+1/2)\pi$ for integer n. Finally, we compute the subgap tunneling conductance of a normal-metal-magnetic film-superconductor junctions on the surface of a topological insulator and show that the position of the peaks of the zero-bias tunneling conductance can be tuned using the magnetization of the ferromagnetic film. We point out that these phenomena have no analogs in either conventional two-dimensional materials or Dirac electrons in graphene and suggest experiments to test our theory.

DOI: 10.1103/PhysRevB.82.045120 PACS number(s): 71.10.Pm, 73.20.−r

I. INTRODUCTION

Topological insulators with time-reversal symmetry in two and three dimensions (2D and 3D) have been studied extensively in recent years, both theoretically and experimentally.[1–9] The 3D topological insulators can be characterized by four integers ν_0 and $\nu_{1,2,3}$.[4] The first integer specifies the class of topological insulators as strong ($\nu_0=1$) or weak ($\nu_0=0$) while the last three integers characterize the time-reversal invariant momenta of the system given by $\vec{M}_0=(\nu_1\vec{b}_1,\nu_2\vec{b}_2,\nu_3\vec{b}_3)/2$, where $\vec{b}_{1,2,3}$ are reciprocal-lattice vectors. The topological features of strong topological insulators (STI) are robust against the presence of time-reversal invariant perturbations such as disorder and lattice imperfections. It has been theoretically predicted[1,4] and experimentally verified[2] that the surface of a STI has an odd number of Dirac cones whose positions are determined by the projection of $\vec{M}_0$ on to the Brillouin zone of the surface. The position and number of these cones depend on both the nature of the surface concerned and the integers $\nu_{1,2,3}$. For compounds such as HgTe and Bi_2Se_3, specific surfaces with a single Dirac cone near the Γ point of the 2D Brillouin zone have been found.[2,7,9] Such a Dirac cone is described by the Hamiltonian

$$H=\int \frac{dk_x dk_y}{(2\pi)^2}\psi^\dagger(\vec{k})(\hbar v_F\vec{\sigma}\cdot\vec{k}-\mu I)\psi(\vec{k}), \tag{1}$$

where $\vec{\sigma}(I)$ denotes the Pauli (identity) matrices in spin space, $\psi=(\psi_\uparrow,\psi_\downarrow)^T$ is the annihilation operator for the Dirac spinor (T denotes the transpose of a row vector), v_F is the Fermi velocity, and μ is the chemical potential.[10] Recently, several novel features of these surface Dirac electrons such as the existence of Majorana fermions in the presence of a magnet-superconductor interface on the surface,[10,11] generation of time-reversal symmetric p_x+ip_y-wave superconducting state via proximity to a s-wave superconductor,[10] anomalous magnetoresistance of ferromagnet-ferromagnet junctions,[12] and novel spin textures with chiral properties[9] have been studied in detail. Further it has been shown in Ref. 13 that it is possible to realize a magnetic switch by magnetically tuning the transport of Dirac fermions with a proximate ferromagnetic film. However, the response of these fermions in the presence of crossed electric and magnetic fields has not been studied so far. Another aspect of such fermions, namely, their transport through a normal-metal-magnetic film-superconductor (NMS) junction has also not been explored.

In this work, we study several magnetotransport properties of these surface Dirac fermions in experimentally realizable situations. We first study the properties of the fermions in the presence of crossed magnetic $[\vec{B}=(0,B\cos\theta,B\sin\theta)]$ and electric fields $[\vec{\mathcal{E}}=(\mathcal{E},0,0)]$ as shown in Fig. 1. We present an exact solution of this problem and show that for $\beta=\mathcal{E}/(v_FB\sin\theta)\leq 1$, the relative contributions of the Zeeman and the orbital terms to the Landau-level energies, and hence their magnetic field dependence, can be tuned by varying either the strength of the applied electric field or the tilt of the applied magnetic field. We also show that for $\mathcal{E}>v_FB\sin\theta$, the conductance of these Dirac fermions has an unconventional dependence on the tilt angle θ of the applied magnetic field and that this dependence can be used to realize electric field controlled switching.

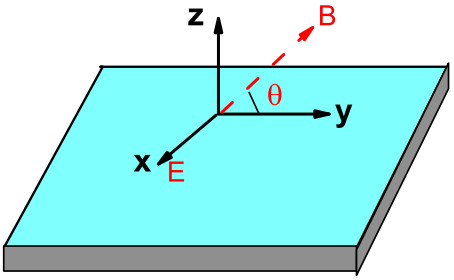

FIG. 1. (Color online) Schematic representation of the crossed electric and magnetic field geometry. The electric field is applied along x while the magnetic field is in the y-z plane. See text for details.

The second study involves an extension of the results obtained in Ref. 13 regarding transport in normal-metal-magnetic film-normal metal (NMN) and normal-metal-barrier-magnetic film (NBM) junctions of topological insulators. The relevant experimental geometries are shown in Fig. 2. We study the transport of these Dirac electrons across a region with a width d where there is a proximity-induced exchange field $\mathcal{J}$ arising from the magnetization $\vec{m}=m_0\hat{y}$ of a proximate ferromagnetic film as shown in the left panel of Fig. 2. We demonstrate that the tunneling conductance G of these Dirac fermions through such a junction can either be an oscillatory or a monotonically decaying function of the junction width d. One can interpolate between these two qualitatively different behaviors of G by changing m_0 (and thus $\mathcal{J}$) by an applied in-plane magnetic field leading to the possible use of this junction as a magnetic switch. We also study the transport properties of Dirac fermions across a barrier characterized by a width d and a potential V_0 in region II with a magnetic film proximate to region III as shown in the right panel of Fig. 2. We note that it is well known from the context of Dirac fermions in graphene[14] that such a junction, in the absence of the induced magnetization, exhibits transmission resonances with maxima of transmission at $\chi=eV_0d/\hbar v_F=n\pi$, where n is an integer. Here we show that beyond a critical strength of m_0, the maxima of the transmission shifts to $\chi=(n+1/2)\pi$. Upon further increasing m_0, one

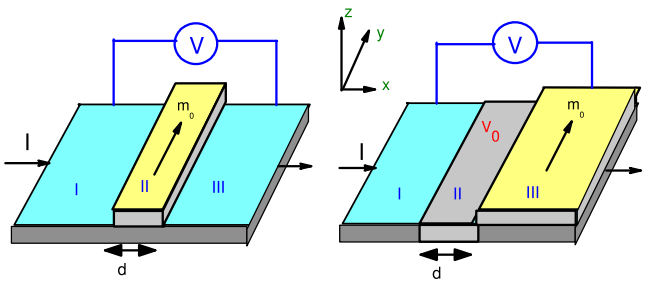

FIG. 2. (Color online) Proposed experimental setups. Left panel: schematic representation of a NMN junction. The ferromagnetic film extends over region II of width d providing an exchange field in this region. Right panel: schematic representation of a NBM junction. The film extends over region III while the region II has a barrier characterized by a voltage V_0. V and I denote the bias voltage and current across the junctions, respectively. See text for details.

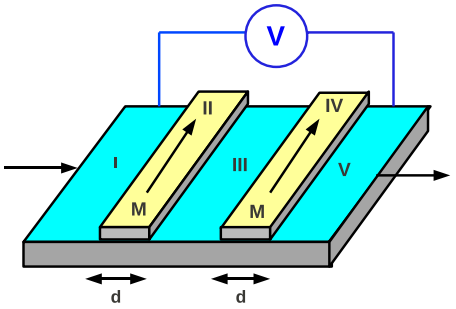

FIG. 3. (Color online) Schematic representation of multiple NMN junction with two magnetic regions. The ferromagnetic film extends over regions II and IV, both of width d. Regions I, III, and V are normal topological insulator surfaces.

can reach a regime where the conductance across the junctions vanishes. We also point out that such NMN and NBM junctions can be used to determine the exact form of the Dirac Hamiltonian on the surface of the topological insulator. We also present a transfer-matrix formalism to analyze multiple NMN junction with N regions [out of which $(N-1)/2$ regions have induced magnetization due to proximity of a magnetic film] with width d and magnetization M as shown in Fig. 3 for $N=5$.

Finally, we study the transport of Dirac fermions across a NMS junction as shown in Fig. 4. The intermediate region (region II) in this junction has a thickness d with a proximate ferromagnetic film providing a magnetization M while superconductivity is introduced in region III via the proximity effect. We provide a detailed analysis of the subgap tunneling conductance G of these NMS junctions as a function of the applied voltage V and magnetization M. In particular, we point out that the positions of the maxima of the zero-bias tunneling conductance in such NMS junctions as a function of the width d of the magnetic film can be varied by tuning the induced magnetization M. We stress that the properties of the Dirac fermions elucidated in all these studies are a consequence of their spinor structure in physical spin space and thus have no analogs for either conventional Schrödinger electrons in 2D or Dirac electrons in graphene.[15–17]

The organization of the rest of the paper is as follows. In Sec. II, we study the properties of the Dirac fermions in the

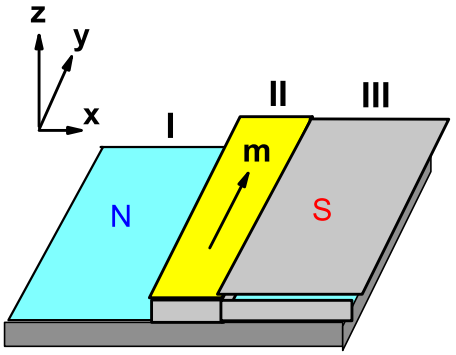

FIG. 4. (Color online) Schematic representation of the NMS junction. The ferromagnetic film is on region II while superconductivity is induced in region III via a proximate superconducting film. See text for details.

presence of crossed electric and magnetic fields. This is followed by the study of NMN and NBM junctions of these Dirac materials in Sec. III. In Sec. IV, we study the transport properties and subgap tunneling conductance of NMS junctions of topological insulators. Finally we discuss possible experimental verification of theory and conclude in Sec. V.

II. CROSSED ELECTRIC AND MAGNETIC FIELDS

We begin with the properties of Dirac electrons in a crossed electric and magnetic field as shown in Fig. 1. The Hamiltonian for the Dirac fermions for this case can be written as

$$H = \int d^2 r \psi^\dagger(\vec{r})[v_F \vec{\sigma}\cdot\Pi - \mu I - g\mu_B \vec{\sigma}\cdot\vec{B} - e\mathcal{E}x]\psi(\vec{r}), \quad (2)$$

where $\vec{\Pi}=-i\hbar\vec{\nabla}-e\vec{A}$ is the canonical momentum, c is set to unity, g is the gyromagnetic ratio, μ_B is the Bohr magneton, and we choose the vector potential to be $\vec{A}=(0, Bx\sin\theta, -Bx\cos\theta)$. Note that here the Zeeman term does not determine the spin-quantization axis of the Dirac electrons due to the presence of the $\vec{\Pi}$ term. Since the z component of the vector potential plays no role in the Hamiltonian, the in-plane component of the magnetic field, $B\cos\theta$, enters the Hamiltonian only through the σ_y piece in the Zeeman term; further, this can be removed by a gauge transformation by shifting k_y by a constant. This property of the Dirac fermions is distinct from its counterpart in graphene. For $\mathcal{E}=0$, Eq. (2) admits a straightforward solution and yields the Landau-level spectrum

$$E_n = \pm \hbar v_F l_B^{-1}\sqrt{2|n| + \alpha B\sin\theta} \text{ if } n \neq 0,$$

$$= -|g\mu_B B\sin\theta| \text{ if } n = 0, \quad (3)$$

where $\alpha = g^2\mu_B^2/\hbar v_F^2 e$, $l_B = \sqrt{\hbar/[eB\sin\theta]}$ is the magnetic length and we also define $l_B^0 = l_B(\theta=\pi/2)$ for later use. The $n=0$ state is nondegenerate as is also known from analogous studies of Landau levels in graphene.[14] For the Dirac electrons on the surface of Bi_2Se_3, $v_F \simeq 6\times 10^5$ m/s,[6] so that $\alpha \simeq 10^{-4}/T$ leading to a negligible contribution of the Zeeman term in the spectrum.

The situation changes when an electric field is applied along x. In this case, for $\mathcal{E} \leq v_F B\sin\theta$, one can define a boost parameter $\beta = \mathcal{E}/[v_F B\sin\theta] \leq 1$ and carry out a Lorentz transformation[18]

$$x' = x, \quad y' = \gamma(y + \beta v_F t), \quad t' = \gamma(t + \beta y/v_F),$$

$$\mathcal{E}' = \gamma(\mathcal{E} - \beta B\sin\theta),$$

$$B'\sin\theta' = \gamma(B\sin\theta - \beta\mathcal{E}),$$

$$\psi'(\vec{r}') = \exp[-\sigma_y \operatorname{arctanh}(\beta)/2]\psi(\vec{r}), \quad (4)$$

where $\gamma = (1-\beta^2)^{-1/2}$. In the boosted frame the Dirac equation reads

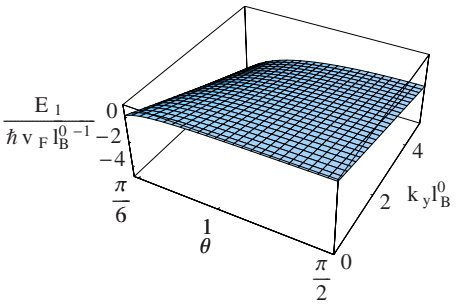

FIG. 5. (Color online) Plot of Landau-level energy E_n for $n=1$ as a function of the tilt angle θ and transverse momentum k_y for a fixed electric field $\mathcal{E}=0.5v_F B$. Note that $\theta=\pi/6$ corresponds to $\beta=1$.

$$E_n'\psi' = \left\{ -i\hbar v_F\left[\sigma_x\partial_x + \sigma_y\left(\partial_{y'} - i\frac{eB'\sin\theta'}{v_F}x\right)\right] - g\mu_B\sigma_z B\sin\theta\right\}\psi'. \quad (5)$$

Note that such a boost transformation leaves the out-of-plane Zeeman field unchanged. The energy eigenvalues of Eq. (5) can be easily obtained and are given by

$$E_n' = \pm\hbar v_F l_B'^{-1}\sqrt{2|n| + \alpha B\sin\theta} \text{ if } n \neq 0,$$

$$= -|g\mu_B B\sin\theta| \quad \text{if } n = 0, \quad (6)$$

where $l_B' = \sqrt{\hbar/[eB'\sin\theta']}$. Then a reverse boost to the "laboratory" frame yields

$$E_n(k_y) = \pm\hbar v_F l_B^{-1}\gamma^{-3/2}\sqrt{2|n| + \alpha B\gamma\sin\theta} - \beta\hbar v_F k_y \text{ if } n \neq 0,$$

$$= -\gamma^{-1}|g\mu_B B\sin\theta| - \beta\hbar v_F k_y \text{ if } n = 0. \quad (7)$$

Equation (7) is one of the central results of this section. It demonstrates that a collapse of the Landau levels for the Dirac fermions can be induced by varying either the electric field for a fixed tilt of the applied magnetic field or by varying the magnetic field tilt for a fixed electric field. A plot of the energy level as a function of this tilt and the transverse momentum k_y is shown in Fig. 5.

We also note that the magnetic field dependence of the Landau-level energy gaps are different from their counter part in graphene. To illustrate this we define $\Delta_n = E_{n+1}(k_y) - E_n(k_y)$ for $n \neq 0$. For $\beta \ll 1$, we find

$$\frac{\Delta_n}{\hbar v_F l_B^{0-1}} \simeq \gamma^{-3/2}\sqrt{\sin(\theta)}(\sqrt{2|n+1|} - \sqrt{2|n|}). \quad (8)$$

For $\beta \simeq 1$ when $\gamma\alpha B \gg |n|$, we find that $\Delta_n/(\hbar v_F l_B^{0-1}) \simeq \gamma^{-3/2}/(2\sqrt{\alpha B\gamma})$. This behavior is distinct from its counter part in graphene where $\Delta_n/(\hbar v_F l_B^{0-1}) = \gamma^{-3/2}\sqrt{\sin\theta}(\sqrt{n+1} - \sqrt{n})$ for all B. However, since $\alpha \sim 10^{-4}/\mathrm{T}$, this behavior can only be seen in a very tiny window near critical tilt and would be hard to figure out in experiments. On the contrary, the variation in dispersion of Δ_n with the tilt angle θ, seen in Fig. 6 for several n, can be tested experimentally with mi-

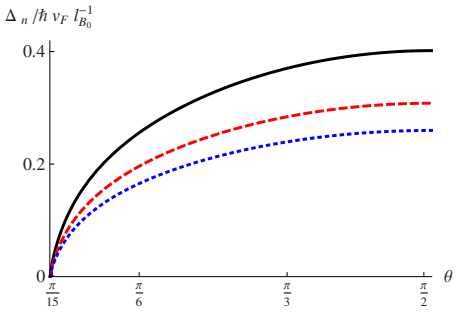

FIG. 6. (Color online) Plot of Landau-level energy gap Δ_n for $n=1$ (black solid line), 2 (red long-dashed line), and 3 (blue dashed line) as a function of the tilt angle θ for a fixed electric field $\mathcal{E}=0.2v_FB$.

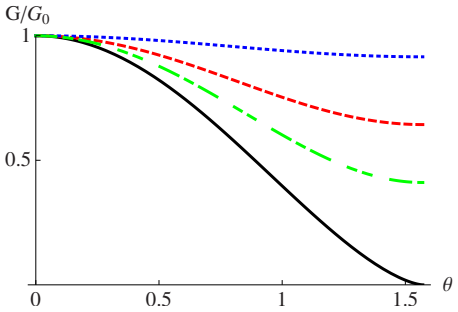

FIG. 7. (Color online) Plot of the conductance G/G_0 as a function of the tilt angle θ for electric field $\mathcal{E}/v_FB=1$ (black solid line), 1.2 (green dashed-dotted line), 1.5 (red long-dashed line), 3 (blue dashed line) for a fixed magnetic field B.

crowave absorption experiments routinely done for conventional quantum Hall systems.[19] This will be discussed further in Sec. V.

Now we turn to the solution of this problem in the regime $\mathcal{E}\geq v_FB$ where we get scattering states. In this regime, we define a parameter $\beta'=v_FB\sin\theta/\mathcal{E}$ and perform a similar boost transformation as outlined earlier. This allows us to shift to a reference frame where there is no magnetic field and the Dirac equation, in the momentum representation, reads[20]

$$ie\mathcal{E}'\hbar\partial_{k_x}\psi' = [\hbar v_F(\sigma_x k_x + \sigma_y k_y) - E' - g\mu_B\sigma_z B\sin\theta]\psi', \tag{9}$$

where $\mathcal{E}'=\gamma'(\mathcal{E}-\beta' v_FB\sin\theta)$ and $E'=\gamma'(E-\hbar v_F k_y\beta')$ are the electric field and energy as seen in the boosted frame, and $\gamma'=1/\sqrt{1-\beta'^2}$. The scattering states can now be easily obtained from this equation by noting the similarity of this equation with the standard Landau-Zener problem with modified Planck's constant $\hbar\to e\mathcal{E}'\hbar$. In particular, the transmission probability of these Dirac electrons in the direction of the applied electric field in the boosted frame can be written as

$$T(k_y;E) = e^{-\pi d_0^2\gamma'[(g\mu_B B\sin\theta)^2+(\hbar v_F k_y')^2]/(\hbar v_F)^2}, \tag{10}$$

where $d_0=\sqrt{\hbar v_F/(e\mathcal{E})}$ is the length scale set by the electric field. Now one can rotate back to the "laboratory frame" using $k_y'=\gamma'(k_y-\beta'\epsilon/\hbar v_F)$ and integrate over k_y modes to obtain the tunneling conductance[20]

$$G = G_0(1-\beta'^2)^{3/4}e^{-\pi\gamma' d_0^2(g\mu_B B\sin\theta)^2/(\hbar v_F)^2}, \tag{11}$$

where $G_0=e^2L_y/(hd_0)$ and L_y is the sample width. We find that in contrast to graphene,[20] the Zeeman term arising from the magnetic field along z produces an additional exponential suppression of the conductance. This can be understood by noting that in topological insulators, a Zeeman magnetic field along z results in the generation of a mass term for the Dirac electrons and hence leads to a suppression of the conductance. A plot of G/G_0 as a function of the tilt of a magnetic field θ is shown in Fig. 7 for several representative values of the electric field $\mathcal{E}$ and for a fixed magnetic field B. The plot shows that for small electric fields, the conductance is quickly suppressed as we increase θ from 0 to $\pi/2$; however, for larger fields, the suppression is minimal. Thus one can tune the conductance of these insulators either by tuning the electric field at a fixed θ or by tuning θ at a fixed electric field.

III. TRANSPORT IN NMN AND NBM JUNCTIONS

In this section, we analyze the properties of NMN and NBM junctions of topological insulators as shown in the left and right panels of Fig. 2. Section III A discusses the NMN junctions while Sec. III B elucidates the properties of the NBM junctions.

A. NMN junctions

The proposed experimental set up for the NMN junction is shown in the left panel of Fig. 2. The Dirac fermions in region I and III are described by the Hamiltonian in Eq. (1). Consequently, the wave functions of these fermions moving along $\pm x$ in these regions for a fixed transverse momentum k_y and energy ϵ can be written as

$$\psi_j^{\pm} = (1, \pm e^{\pm i\alpha})\exp[i(\pm k_x x + k_y y)], \tag{12}$$

where j takes values I and III, and

$$\alpha = \arcsin(\hbar v_F k_y/|\epsilon+\mu|),$$

$$k_x(\epsilon) = \sqrt{[(\epsilon+\mu)/\hbar v_F]^2 - k_y^2}. \tag{13}$$

In region II, the presence of the ferromagnetic strip with a magnetization $\vec{m}_0=m_0\hat{y}$ leads to the additional term

$$H_{\text{induced}} = \int dxdy\mathcal{J}\theta(x)\theta(d-x)\psi^{\dagger}(\vec{r})\sigma_y\psi(\vec{r}), \tag{14}$$

where $\mathcal{J}\sim m_0$ is the exchange field due to the presence of the strip[12] and $\theta(x)$ denotes the Heaviside step function. Note that H_{induced} may be thought as a vector potential term arising due to a fictitious magnetic field $\vec{B}_f=(\mathcal{J}/ev_F)[\delta(x)-\delta(d-x)]\hat{z}$. This analogy shows that our choice of the in-plane magnetization along $\hat{y}$ is completely general; all gauge-invariant quantities such as the transmission probability are independent of the x component of $\vec{m}_0$ in the present geometry. We emphasize that this effect is distinct from that due to

a finite z component of $\vec{m}_0$ which provides a mass to the Dirac electrons. For a given m_0, the precise magnitude of $\mathcal{J}$ depends on the exchange coupling of the film and can be tuned, for soft ferromagnetic films, by an applied field.[12] The wave function for the Dirac fermions in region II moving along $\pm x$ in the presence of such an exchange field is given by

$$\psi_{\mathrm{II}}^{\pm} = (1, \pm e^{\pm i\beta})\exp[i(\pm k_x' x + k_y y)], \tag{15}$$

where

$$\beta = \arcsin[\hbar v_F(k_y + M)/|\epsilon + \mu|], \quad M = \mathcal{J}/(\hbar v_F),$$

$$k_x'(\epsilon) = \sqrt{[(\epsilon+\mu)/\hbar v_F]^2 - (k_y + M)^2}. \tag{16}$$

Note that beyond a critical $M_c = \pm 2|\epsilon+\mu|/(\hbar v_F)$ and hence a critical $\mathcal{J}_c = \pm 2|\epsilon+\mu|$, k_x' becomes imaginary for all k_y leading to spatially decaying modes in region II.

Let us now consider an electron incident on region II from the left with a transverse momentum k_y and energy ϵ. Taking into account reflection and transmission processes at $x=0$ and $x=d$, the wave function of the electron can be written as

$$\psi_{\mathrm{I}} = \psi_{\mathrm{I}}^{+} + r\psi_{\mathrm{I}}^{-}, \quad \psi_{\mathrm{II}} = p\psi_{\mathrm{II}}^{+} + q\psi_{\mathrm{II}}^{-}, \quad \psi_{\mathrm{III}} = t\psi_{\mathrm{III}}^{+}. \tag{17}$$

Here r and t are the reflection and transmission amplitudes, and p and (q) denotes the amplitude of right (left) moving electrons in region II. Matching boundary conditions on ψ_{I} and ψ_{II} at $x=0$ and ψ_{II} and ψ_{III} at $x=d$ leads to

$$1 + r = p + q, \quad e^{i\alpha} - re^{-i\alpha} = pe^{i\beta} - qe^{-i\beta},$$

$$te^{ik_x d} = pe^{ik_x' d} + qe^{-ik_x' d},$$

$$te^{i(k_x d+\alpha)} = pe^{i(k_x' d+\beta)} - qe^{-i(k_x' d+\beta)}. \tag{18}$$

Solving for t from Eq. (18), one finally obtains the conductance

$$G = dI/dV = (G_0/2)\int_{-\pi/2}^{\pi/2} d\alpha T\cos\alpha. \tag{19}$$

Here $G_0 = \rho(eV)we^2/(\pi\hbar^2 v_F)$, $\rho(eV) = |(\mu+eV)|/[2\pi(\hbar v_F)^2]$ is the density of states of the Dirac fermions and is a constant for $\mu \gg eV$, w is the sample width, and the transmission $T = |t|^2$ is given by

$$T = \cos^2(\alpha)\cos^2(\beta)/[\cos^2(k_x' d)\cos^2(\alpha)\cos^2(\beta) + \sin^2(k_x' d)(1 - \sin\alpha\sin\beta)^2]. \tag{20}$$

Equation (20) and the expression for G represent one of the main results of this section. We note that for a given α, T has an oscillatory (monotonically decaying) dependence on d provided k_x' is real (imaginary). Since k_x' depends, for a given α, on M, we find that one can switch from an oscillatory to a monotonically decaying d dependence of transmission in a given channel (labeled by k_y or equivalently, α) by turning on a magnetic field which controls m_0 and hence M. Also since $-1 \le \sin\alpha \le 1$, we find that beyond a critical $M = M_c$, the transmission in all the channels exhibits a monotonically decaying dependence on d. Consequently, for a thick enough junction one can tune G at fixed V and μ from a finite value to nearly zero by tuning M (i.e., m_0) through M_c. Thus such a junction may be used as a magnetic switch. These qualitatively different behaviors of the junction conductance G for M below and above M_c is demonstrated in Fig. 8 by plotting G as a function of the effective barrier width $z = d|eV + \mu|/\hbar v_F$ for several representative values of $\hbar v_F M/|eV+\mu|$. Since T and hence G depends on M through the dimensionless parameter $\hbar v_F M/|eV+\mu|$, this effect can also be observed by varying the applied voltage V for a fixed μ, d, and M. In that case, for a reasonably large dimensionless barrier thickness $z_0 = d\mu/\hbar v_F$, G/G_0 becomes finite only beyond a critical voltage $|eV_c + \mu| = \hbar v_F M/2$ as shown in Fig. 9 for several representative values of z_0. The critical voltage V_c can be determined numerically by finding the lowest voltage for which G/G_0 exhibits a monotonic decay as a function of z_0. The plot of eV_c/μ as a function of $\hbar v_F M/\mu$, shown in the inset of Fig. 9, demonstrates the expected linear relationship between V_c and M. We note that such a dependence of G on M or V requires the Dirac electrons to be spinors in physical spin space, and is therefore impossible to achieve in either graphene[14] or in a conventional 2D electron gas for which a

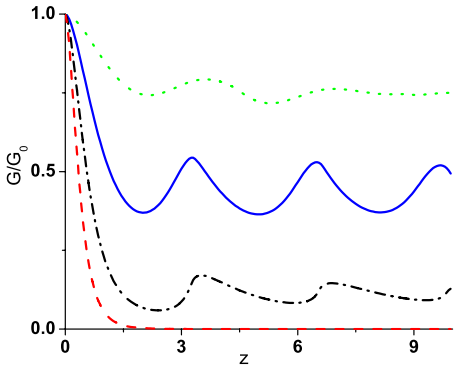

FIG. 8. (Color online) Plot of tunneling conductance G/G_0 for a fixed V and μ as a function of the effective width $z = d|eV + \mu|/\hbar v_F$ for $\hbar v_F M/|eV+\mu| = 0.3$ (green dotted line), 0.7 (blue solid line), 1.3 (black dashed-dotted line), and 2.1 (red dashed line). The value of the critical M is given by $\hbar v_F M/|eV+\mu| = 2$.

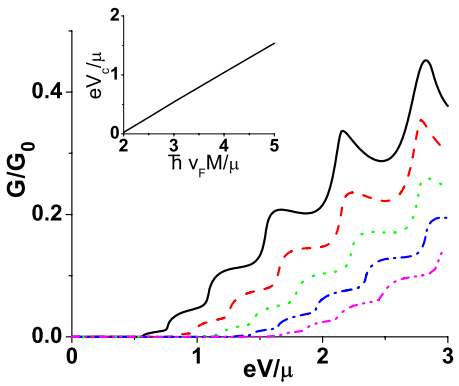

FIG. 9. (Color online) Plot G/G_0 versus eV/μ for several representatives values $\hbar v_F M/\mu$ ranging from 3 (left-most black solid curve) to 5 (rightmost magenta dashed-double dotted line) in steps of 0.5 The effective junction width $z_0 = 5$ for all plots. The inset shows a plot of eV_c/μ versus $\hbar v_F M/\mu$. See text for details.

proximate ferromagnetic film would only provide a Zeeman term for the electrons, leaving G unaffected.

B. NBM junctions

Next, we analyze the NBM junction shown in the right panel of Fig. 2 where the region III below a ferromagnetic film is separated from region I by a potential barrier in region II. Such a barrier can be applied by changing the chemical region in region II either by a gate voltage V_0 or via doping.[7] We will analyze the problem in the thin barrier limit in which $V_0 \to \infty$ and $d \to 0$, keeping the dimensionless barrier strength $\chi = eV_0 d/(\hbar v_F)$ finite. The wave function of the Dirac fermions moving along $\pm x$ with a fixed momentum k_y and energy ϵ in this region is given by

$$\psi'^{\pm}_{\rm II} = (1, \pm e^{\pm i\gamma}) \exp[i(\pm k''_x x + k_y y)/\sqrt{2}], \tag{21}$$

where

$$\gamma = \arcsin(\hbar v_F k_y/|\epsilon + eV_0 + \mu|),$$

$$k''_x(\epsilon) = \sqrt{[(\epsilon + eV_0 + \mu)/\hbar v_F]^2 - k_y^2}. \tag{22}$$

The wave functions in region I and III are given by $\psi'_{\rm I} = \psi_{\rm I}$ and $\psi'_{\rm III} = \psi_{\rm II}$, where $\psi_{\rm I}$ and $\psi_{\rm II}$ are given in Eq. (17). Note that one can have a propagating solution in region III only if $|M| \le |M_c|$.

The transmission problem for such a junction can be solved by a procedure similar to the one outlined above for the magnetic strip problem. For an electron approaching the barrier region from the left, we write down the following forms of the wave function in the three regions I, II, and III: $\psi'_{\rm I} = \psi'^{+}_{\rm I} + r_1 \psi'^{-}_{\rm I}$, $\psi'_{\rm II} = p_1 \psi'^{+}_{\rm II} + q_1 \psi'^{-}_{\rm II}$, and $\psi'_{\rm III} = t_1 \psi'^{+}_{\rm II}$. As outlined earlier, one can then match boundary conditions at $x=0$ and $x=d$, and obtain the transmission coefficient $T_1 = |t_1|^2 k'_x/k_x$ as

$$T_1 = 2\cos\beta\cos\alpha/[1 + \cos(\beta - \alpha) - \cos^2(\chi)\{\cos(\beta - \alpha) - \cos(\beta + \alpha)\}]. \tag{23}$$

Note that in the absence of the ferromagnetic film over region III, $\beta = \alpha$, and $T_1 \to T_1^0 = \cos^2(\alpha)/[1 - \cos^2(\chi)\sin^2(\alpha)]$. The expression for T_1^0, reproduced here for the special case of $M=0$, is well known from analogous studies in the context of graphene, and it exhibits both the Klein paradox ($T_1^0 = 1$ for $\alpha = 0$) and transmission resonances ($T_1^0 = 1$ for $\chi = n\pi$).[15] When $M \neq 0$, we find that the transmission for normal incidence ($k_y = 0$) does become independent of the barrier strength but its magnitude deviates from unity

$$T_1^{\rm normal} = \frac{2\sqrt{1 - (\hbar v_F M/|eV + \mu|)^2}}{1 + \sqrt{1 - (\hbar v_F M/|eV + \mu|)^2}}. \tag{24}$$

The value of $T_1^{\rm normal}$ decreases monotonically from 1 for $M=0$ to 0 for $|M| = |eV + \mu|/(\hbar v_F)$ and can thus be tuned by changing M (or V) for a fixed V (or M) and μ.

The conductance of this junction is given by $G_1 = (G_0/2)\int_{-\alpha_1}^{\alpha_2} d\alpha T_1 \cos\alpha$, where $\alpha_{1,2}$ are determined from the solution of $\cos\beta = 0$ for a given M. A plot of G_1 as a function of $\hbar v_F M/|eV + \mu|$ and χ (for a fixed eV and μ) is shown in Fig. 10. We find that the amplitude of G_1 decreases monotonically as a function of $|M|$ reaching 0 at $M = M_c$ beyond which there are no propagating modes in region III. Also, as we increase M, the conductance maxima shifts from $\chi = n\pi$ to $\chi = (n + 1/2)\pi$ beyond a fixed value of $M^*(V) \simeq \pm c_0|eV + \mu|/(\hbar v_F)$ as shown in the top left panel of Fig. 11. Numerically, we find $c_0 = 0.7075$. At $M = M^*$, $G_1(\chi = n\pi) = G_1[\chi = (n + 1/2)\pi]$, leading to a period halving of $G_1(\chi)$ from π to $\pi/2$. This is shown in the top right panel of Fig. 11 where $G_1(M = M^*)$ is plotted as a function of χ. We note that near M^*, the amplitude of oscillation of G_1 as a function of χ becomes very small so that G_1 is almost independent of χ. In the bottom left panel of Fig. 11, we plot $\chi = \chi_{\rm max}$ (the value of χ at which the first conductance maxima occurs) as a function of $\hbar v_F M/|eV + \mu|$ which clearly demonstrates the shift. This is further highlighted by plotting $\Delta G_1 = G_1(\chi = 0) - G_1(\chi = \pi/2)$ as a function of $\hbar v_F M/|eV + \mu|$ in the bottom right panel of Fig. 11. ΔG_1 crosses zero at $M = M^* < M_c$ indicating the position of the period halving. Thus the

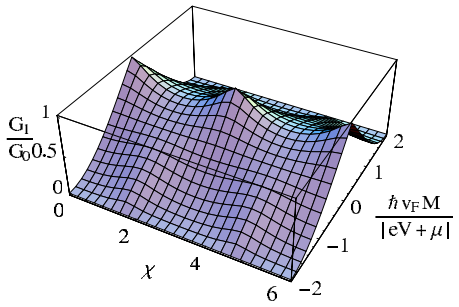

FIG. 10. (Color online) Plot of tunneling conductance G_1/G_0 versus χ and M for a fixed applied voltage V and chemical potential μ. G_1 vanishes for $|M| \ge M_c = 2|eV + \mu|/\hbar v_F$.

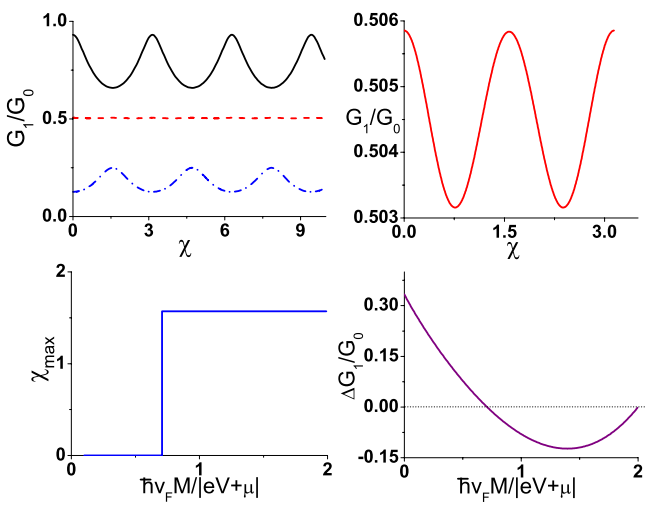

FIG. 11. (Color online) Top left panel: plot of G_1/G_0 versus χ for $\hbar v_F M/|eV + \mu| = 0.1$ (black solid line), 0.7075 (red dashed line), and 1.4 (blue dashed-dotted line) for fixed V and μ. Top right panel: plot of G_1/G_0 versus χ at $M = M^*$ showing the period halving. Bottom left panel: plot of $\chi_{\rm max}$ versus $\hbar v_F M/|eV + \mu|$ showing conductance maxima positions. Bottom right panel: plot of $\Delta G_1/G_0$ versus $\hbar v_F M/|eV + \mu|$ which crosses 0 at $M = M^*$. The dotted line is a guide to the eyes.

position of the conductance maxima depends crucially on $\hbar v_F M/(eV+\mu)$ and can be tuned by changing either M or V.

C. Alternative forms of the Hamiltonian

In this section, we discuss a possible way of distinguishing between possible forms of the Dirac Hamiltonian in the surface of a topological insulator. In the literature (see, for instance, Ref. 21), two such different forms have been studied for the first part of the Hamiltonian in Eq. (1), namely,

$$h_1 = \int \frac{d^2k}{(2\pi)^2} \psi^\dagger(\vec{k}) \hbar v_F (\sigma_x k_x + \sigma_y k_y) \psi(\vec{k})$$

and

$$h_2 = \int \frac{d^2k}{(2\pi)^2} \psi^\dagger(\vec{k}) \hbar v_F (\sigma_x k_y - \sigma_y k_x) \psi(\vec{k}). \tag{25}$$

We have implicitly assumed the form h_1 in the entire analysis in this paper. We note that h_1 and h_2 are both time-reversal invariant since $\vec{\sigma} \to -\vec{\sigma}$ and $\vec{k} \to -\vec{k}$ under that transformation and they are also invariant under rotations in the x-y plane. But they transform differently under a parity transformation. Let us introduce the z coordinate for the moment and define the parity transformation as $x \to -x$, $y \to y$, and $z \to z$. Hence, $k_x \to -k_x$, $k_y \to k_y$, and $k_z \to k_z$. Since $\vec{\sigma}$ transforms in the same way as orbital angular momentum $\vec{r} \times \vec{k}$, we see that $\sigma_x \to \sigma_x$ and $\sigma_y \to -\sigma_y$. Hence $h_1 \to -h_1$ while $h_2 \to h_2$ under parity. Since the Hamiltonian of the surface Dirac electrons arises from a spin-orbit coupling in the bulk which is then projected on to the two-dimensional surface, and we have not discussed the bulk Hamiltonian here, we have no *a priori* reason to choose between h_1 and h_2. In principal, we could even consider a linear combination of the two such as $\cos\theta h_1 + \sin\theta h_2$. Clearly, when an in-plane magnetization which breaks the in-plane rotational symmetry is introduced using the ferromagnetic film, the effect of this on the analysis in Secs. III A and III B will depend on the angle θ mentioned above; for instance, a magnetization in the y direction will couple to σ_y and will therefore shift the momentum k_y for h_1 and k_x for h_2. Hence, when experimental tests of the various results obtained in those two sections are performed, one can probe whether the Hamiltonian for the system of interest is actually h_1 or h_2 or a linear combination of the two, by varying the direction of magnetization of the ferromagnetic film and studying the effect that this has on the conductance. For example, if the Hamiltonian describing the surface electrons of the topological insulator turns out to be h_2, m_y will have no effect on transport. In general, for any θ, there will be specific direction of the in-plane magnetization $\vec{m} \equiv m_y \cos\theta + m_x \sin\theta$ which will have maximal effect on the transport while the component of the magnetization $\vec{m}' = -m_x \cos\theta + m_y \sin\theta$ will not affect the transport at all.

D. Multiple NMN junctions

In this section, we study multiple topological insulator junctions using the transfer-matrix formalism. To this end, we consider multiple topological insulator junctions which consist of N regions with $(N-1)/2$ regions of constant induced magnetization M as shown in Fig. 3 for $N=5$. We denote the extent of these regions to be between $x_1 \le x \le x_2$, $x_2 \le x \le x_3, \ldots, x_{N-1} \le x \le x_N$.

The general Hamiltonian that describes different regions in such junctions can be represented as $H(x) = \sigma^x(-i\partial_x) + \sigma^y[-i\partial_y - A(x)] + V(x)$, where $A(x)$ and $V(x)$ are the vector and scalar potentials, respectively. As before, the x component of the vector potential can be gauged away without any loss of generality. We consider the eigenfunctions in different regions to be $\psi(x,y) = \chi(x)\exp(ik_y y)$, as $H(x)$ has translational invariance along the y direction. Let us first consider a single junction, consisting of three regions. Then from the Dirac equation for this junction we get

$$\{-i\sigma^x \partial_x + \sigma_y[k_y - A(x)] + V(x)\}\chi(x) = E\chi(x). \tag{26}$$

From Eq. (26), the wave function at any position x is given by

$$\chi(x) = \mathcal{P}[e^{-i\int_{x_0}^{x} dx' D(\kappa(x'),\epsilon(x'))}]\chi(x_0), \tag{27}$$

where

$$\kappa(x) = k_y - A(x),$$

$$\epsilon(x) = E - V(x),$$

$$D[\kappa(x),\epsilon(x)] = i\sigma^z \kappa(x) - \sigma^x \epsilon(x),$$

and $\mathcal{P}$ denotes path ordering. Here we consider topological insulator junctions with piecewise constant potentials that are independent of x. Thus Eq. (27) simplifies to $\chi(x) = T(\kappa,\epsilon)\chi(x_0)$, where $T(\kappa,\epsilon) = e^{-iD(\kappa,\epsilon)(x-x_0)}$ represents the transfer matrix for a single junction.

Let us now denote $|\alpha,p\rangle = 1/\sqrt{2}(e^{-i\alpha/2}, pe^{i\alpha/2})$ to be the eigenvectors of the Hamiltonian $H(x)$ and $D(\kappa,\epsilon)$, where $\alpha = \tan^{-1}(\kappa/k_x)$ and $p = \mathrm{sgn}(\epsilon)$. However, since D is non-Hermitian, its left and right eigenvectors are not equal and are given by

$$D(\kappa,\epsilon)|\pi-\alpha,p\rangle = k_x|\pi-\alpha,p\rangle,$$

$$D(\kappa,\epsilon)|\alpha,p\rangle = -k_x|\alpha,p\rangle,$$

$$\langle\alpha-\pi,p|D(\kappa,\epsilon) = k_x\langle\alpha-\pi,p|,$$

$$\langle-\alpha,p|D(\kappa,\epsilon) = -k_x\langle-\alpha,p|.$$

It is then easy to see that D can be written in terms of these eigenvectors as

$$D(\kappa,\epsilon) = k_x\left(\frac{|\pi-\alpha\rangle\langle\alpha-\pi|}{\langle\alpha-\pi|\pi-\alpha\rangle} - \frac{|\alpha\rangle\langle-\alpha|}{\langle-\alpha|\alpha\rangle}\right)$$

$$= \frac{-k_x}{\cos\alpha}\left(\frac{|\pi-\alpha\rangle\langle\alpha-\pi|}{\langle\alpha-\pi|\pi-\alpha\rangle} + \frac{|\alpha\rangle\langle-\alpha|}{\langle-\alpha|\alpha\rangle}\right), \tag{28}$$

where we assume ϵ is positive. Hence, the transfer matrix can be written as

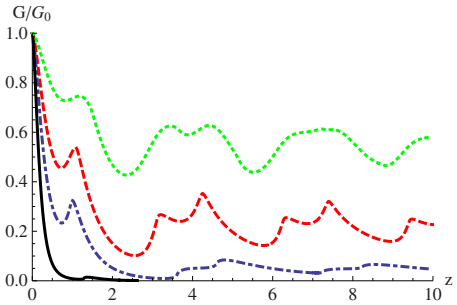

FIG. 12. (Color online) Plot of tunneling conductance for NMN junctions with two magnetic regions showing G/G_0 for a fixed V and μ as a function of the effective width $z=d|eV+\mu|/\hbar v_F$, for magnetization $\hbar v_F M/|eV+\mu|=0.5$ (green dotted line), 1 (red dashed line), 1.5 (blue dotted-dashed line), and 2.5 (black solid line).

$$T(x,x_0)=\frac{1}{\cos\alpha}\left(-\frac{|\pi-\alpha\rangle\langle\alpha-\pi|}{\langle\alpha-\pi|\pi-\alpha\rangle}e^{ik_x x}+\frac{|\alpha\rangle\langle-\alpha|}{\langle-\alpha|\alpha\rangle}e^{-ik_x x}\right). \tag{29}$$

We now apply this formalism to multiple junctions with N regions. For fixed E and k_y, the fields in the nth region can be parameterized by (κ_n,ϵ_n) so that the eigenvector in the $(N+1)$th region can be written as

$$\chi(x_N)=\left(\prod_{n=1}^{N-1}e^{-iD(\kappa_n,\epsilon_n)d_n}\right)\chi(x_1)=T(x_N,x_1)\chi(x_1), \tag{30}$$

where $d_n=x_{n+1}-x_n$. Using Eq. (29), we can write Eq. (30) in terms of the reflected and transmitted wave functions of the barrier region as

$$t|\pi-\alpha_N\rangle e^{ik_{x_N}x_N}=T(x_N,x_1)(|\pi-\alpha_0\rangle e^{ik_{x_0}x_1}+r|\alpha_0\rangle e^{-ik_{x_0}x_1}).$$

The reflection and transmission coefficients can thus be determined in terms of the matrix elements of the transfer matrix as

$$\frac{1}{t}=\frac{-1}{\cos\alpha_0}e^{i(k_{x_N}x_N-k_{x_0}x_1)}\langle\alpha_0-\pi|T^{-1}|\pi-\alpha_N\rangle, \tag{31}$$

$$\frac{r}{t}=\frac{-1}{\cos\alpha_0}e^{i(k_{x_N}x_N+k_{x_0}x_1)}\langle\alpha_0|T^{-1}|\pi-\alpha_N\rangle. \tag{32}$$

We numerically compute these coefficients and hence the conductance of multiple NMN junctions using $G=G_0\int dk_y/(2\pi)|t|^2$. We have verified that this formalism reproduces the results of Secs. III A and III B for a single junction. For $N=5$ and $N=7$ where the junctions consist of two and three magnetic regions, respectively, we plot the variation in G as a function of the effective width $z=d|eV+\mu|/\hbar v_F$ at a fixed applied voltage V for different values of the magnetization M in Figs. 12 and 13. We find that G becomes an exponentially decaying function of the barrier width beyond a critical magnetization as in a single NMN junction. The critical magnetization is the same as that for the single junction ($N=3$ in our notation); however, the barrier width required to achieve near-zero transmission decreases with N. Below the critical magnetization the conductance remains oscillatory; however, the oscillation patterns become more complex with increasing number of junctions.

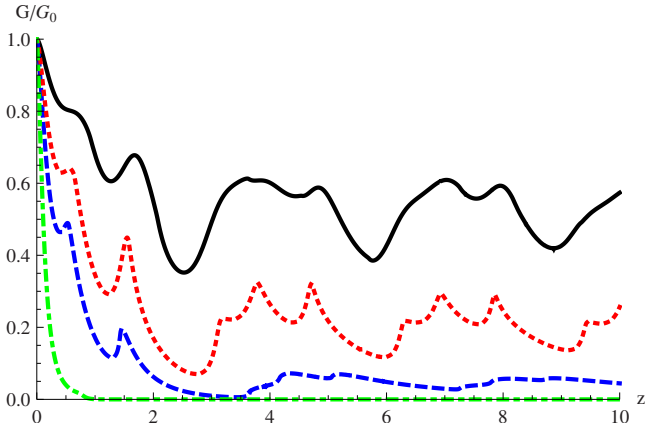

FIG. 13. (Color online) Plot of tunneling conductance for a NMN junction with three magnetic regions showing G/G_0 for a fixed V and μ as a function of the effective width $z=d|eV+\mu|/\hbar v_F$, for magnetization $\hbar v_F M/|eV+\mu|=0.5$ (black solid line), 1 (red dotted line), 1.5 (blue dashed line), and 3 (green dotted-dashed line).

We have left the application of this transfer-matrix formalism to multiple NBM or NMS junctions as a subject of future studies.

IV. TRANSPORT IN NMS JUNCTIONS

We consider a NMS junction on the surface of a topological insulator as shown in Fig. 4. As shown there, region II, which extends from $x=-d$ to $x=0$, has a proximate ferromagnetic film leading to an induced magnetization $\vec{M}=M\hat{y}$. Region III depicts the superconducting region occupying $x>0$. We assume that superconductivity in this regime is induced via a proximate superconducting film with s-wave pairing as shown in the figure. The quasiparticles of such a superconductor can be described by the following Dirac-Bogoliubov-de Gennes (DBdG) equation:[4]

$$\begin{bmatrix}H-E_F & \Delta(r)\\ \Delta^*(r) & E_F-H\end{bmatrix}\psi=E\psi, \tag{33}$$

where $\psi=(\psi_\uparrow,\psi_\downarrow,\psi_\uparrow^\dagger,\psi_\downarrow^\dagger)$ are the four components for the electron and the hole spinors, and the Hamiltonian H is given by

$$H=-i\hbar v_F\vec{\sigma}\cdot\vec{\nabla}+\mu\sigma_y B\theta(x+d)\theta(-x), \tag{34}$$

where $\theta(x+d)$ and $\theta(-x)$ are Heaviside step functions. $\Delta(r)=\Delta_0\exp(i\phi)\theta(x)$ is the BCS pair potential in region III.

Equation (1) can be solved for the normal, magnetic, and superconducting regions. In the normal region, the wave functions for electron and hole moving in $\pm x$ direction are given by

$$\psi_N^{e\pm}=(1,\pm e^{\pm i\alpha},0,0)\exp[i(\pm k_n x+qy)], \tag{35}$$

$$\psi_N^{h\pm}=(0,0,1,\mp e^{\pm i\alpha'})\exp[i(\pm k_n' x+qy)], \tag{36}$$

$$\sin\alpha = \frac{\hbar v_F q}{|\epsilon + E_F|}, \quad \sin\alpha' = \frac{\hbar v_F q}{|\epsilon - E_F|}, \tag{37}$$

where the wave vector $k_n(k_n')$ for the electron (hole) wave functions are given by

$$k_n(k_n') = \sqrt{\left[\frac{\epsilon + (-)E_F}{\hbar v_F}\right]^2 - q^2} \tag{38}$$

and $\alpha(\alpha')$ is the angle of incidence of the electron (hole).

In region II, the wave functions for an electron and a hole moving in the $\pm x$ direction are as follows:

$$\psi_B^{e\pm} = (1, \pm e^{\pm i\theta}, 0, 0)\exp[i(\pm k_b x + qy)], \tag{39}$$

$$\psi_B^{h\pm} = (0, 0, 1, \mp e^{\pm i\theta'})\exp[i(\pm k_b' x + qy)], \tag{40}$$

$$\sin\theta = \frac{\hbar v_F (q + M)}{|\epsilon + E_F|}, \quad \sin\theta' = \frac{\hbar v_F (q + M)}{|\epsilon - E_F|}, \tag{41}$$

where the wave vector $k_b(k_b')$ of the electron (hole) wave function is given by

$$k_b(k_b') = \sqrt{\left[\frac{\epsilon + (-)E_F}{\hbar v_F}\right]^2 - (q + M)^2}. \tag{42}$$

Here $\theta(\theta')$ is the angle of incidence of the electron (hole). Note that, in principle, we could have applied an additional gate voltage V_0 in this region as was done in Ref. 15. However, this leads to an expression of the longitudinal momentum

$$k_b(k_b') = \sqrt{\left[\frac{\epsilon + (-)(E_F - V_0)}{\hbar v_F}\right]^2 - (q + M)^2}. \tag{43}$$

This shows that in the limit of large V_0, the effect of M on $k_b(k_b')$ and hence on G becomes negligible. Therefore we restrict ourselves to the $V_0 = 0$ limit.

In the superconducting region, the BdG quasiparticles are mixtures of electron and holes. Hence the wave function for BdG quasiparticles moving in $\pm x$ directions with transverse momenta q and energy ϵ for $E_F \gg \epsilon, \Delta_0$ are given by

$$\psi_S^{e\pm} = (e^{\mp i\beta}, \mp e^{\pm i(\gamma-\beta)}, e^{-i\phi}, \mp e^{i(\pm\gamma-\phi)}) \times \exp[i(\pm k_s x + qy) - \kappa x], \tag{44}$$

$$\sin\gamma = \frac{\hbar v_F q}{|E_F|}, \quad k_s = \sqrt{\left(\frac{E_F}{\hbar v_F}\right)^2 - q^2}, \tag{45}$$

and $\beta = \cos^{-1}(\epsilon/\Delta_0)\theta(\Delta_0 - \epsilon) - i\cosh^{-1}(\epsilon/\Delta_0)\theta(\epsilon - \Delta_0)$, where θ denotes the Heaviside step function.

Next, we note that for any transmission process to take place we need $\alpha', \theta, \theta', \gamma \leq \pi/2$. This condition gives the limits for the range of α. For simplicity we consider $V_0 = 0$ in region II. Then $\theta' > \theta > \alpha'$. Using Eqs. (37), (41), and (45), we find that the Andreev process takes place for $\alpha_{c1} < \alpha < \alpha_{c2}$, where

$$\alpha_{c1} = \arcsin[(-|\epsilon - E_F|)/|\epsilon + E_F|], \tag{46}$$

$$\alpha_{c2} = \arcsin[(|\epsilon - E_F| - M)/|\epsilon + E_F|]. \tag{47}$$

Note that $\alpha_{c1} \neq -\alpha_{c2}$ and this asymmetry is generated by the induced magnetization M.

Following Ref. 15, we write wave functions for the normal, magnetic, and superconducting regions as

$$\Psi_N = \psi_N^{e+} + r\psi_N^{e-} + r_A\psi_N^{h-}, \tag{48}$$

$$\Psi_B = p\psi_B^{e+} + q\psi_B^{e-} + m\psi_B^{h+} + n\psi_B^{h-}, \tag{49}$$

$$\Psi_S = t\psi_S^{+} + t'\psi_S^{-}, \tag{50}$$

where both normal and Andreev reflection are taken into account. Here r and r_A denote the amplitudes for normal and Andreev reflection, respectively. These wave functions must satisfy the following boundary conditions,

$$\Psi_N|_{x=-d} = \Psi_B|_{x=-d}, \quad \Psi_B|_{x=0} = \Psi_S|_{x=0}. \tag{51}$$

Solving these boundary conditions, we obtain for r, r_A, t and t' (Ref. 15)

$$r = e^{-2ik_n d}N/D, \tag{52}$$

$$N = [e^{i\alpha}\cos(k_b d + \theta) + i\sin(k_b d)] - \rho[\cos(k_b d - \theta) + ie^{i\alpha}\sin(k_b d)], \tag{53}$$

$$D = [e^{-i\alpha}\cos(k_b d + \theta) - i\sin(k_b d)] + \rho[\cos(k_b d - \theta) - ie^{-i\alpha}\sin(k_b d)], \tag{54}$$

$$t' = \frac{1}{\cos(\theta)[\Gamma e^{-i\beta} + e^{i\beta}]}(e^{-ik_n d}[\cos(k_b d - \theta) + ie^{i\alpha}\sin(k_b d)] + re^{ik_n d}[\cos(k_b d - \theta) - ie^{-i\alpha}\sin(k_b d)]), \tag{55}$$

$$t = \Gamma t', \tag{56}$$

$$r_A = \frac{t'(\Gamma + 1)e^{ik_n' d}\cos(\theta')e^{-i\phi}}{\cos(k_b' d - \theta') - ie^{-i\alpha'}\sin(k_b' d)}, \tag{57}$$

where the parameters ρ, Γ, and η can be expressed as

$$\rho = \frac{-\Gamma e^{i(\gamma-\beta)} + e^{-i(\gamma-\beta)}}{\Gamma e^{-i\beta} + e^{i\beta}}, \tag{58}$$

$$\Gamma = \frac{e^{-i\gamma} - \eta}{e^{i\gamma} + \eta}, \tag{59}$$

$$\eta = \frac{e^{-i\alpha'}\cos(k_b' d + \theta') - i\sin(k_b' d)}{\cos(k_b' d - \theta') - ie^{-i\alpha'}\sin(k_b' d)}. \tag{60}$$

The tunneling conductance of the NMS junction can be expressed in terms of r and r_A as

$$\frac{G(eV)}{G_0(eV)} = \int_{\alpha_{c1}}^{\alpha_{c2}} d\alpha\left(1 - |r|^2 + |r_A|^2\frac{\cos\alpha'}{\cos\alpha}\right)\cos\alpha. \tag{61}$$

A plot of the subgap tunneling conductance G/G_0 as a function of the magnetization M and the applied voltage V

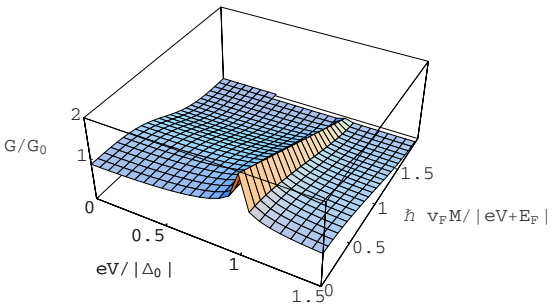

FIG. 14. (Color online) Plot of subgap tunneling conductance $G(V)$ as a function of the induced magnetization M and applied voltage V. See text for details.

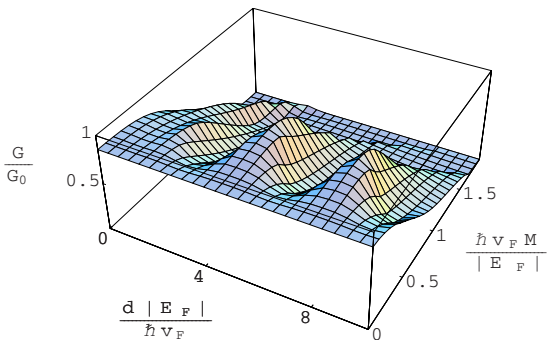

FIG. 15. (Color online) Plot of zero-bias tunneling conductance $G(0)/G_0$ as a function of the induced magnetization M and the barrier width d. See text for details.

for a fixed barrier width d is shown in Fig. 14. We find that $G(0)$ decreases monotonically as a function of the magnetization for all values of the applied voltage. This can be easily attributed to a decrease in the number of conduction channels (i.e., number of k_y modes with real k_b) with increasing M. The behavior of the zero-bias conductance as a function of the barrier width d and magnetization M is shown in Fig. 15. We find that the zero-bias conductance shows an oscillatory behavior as a function of the barrier width d for small M.[22] With increasing M, the position of the conductance maxima shifts which demonstrates the tunability of the zero-bias conductance with the induced magnetization. This continuous shift in position of the zero-bias conductance maxima is to be contrasted with the sudden change in its counterpart in NMN junctions of topological insulators.

V. EXPERIMENTS

Several experimental works on 2D (Ref. 23) and 3D (Refs. 1 and 2) topological insulators have already been carried out. Experimental verification of our work would involve carrying out the following experiments. For a topological insulator in a crossed electric and magnetic field with $\mathcal{E} \leq v_F B \sin(\theta)$, we propose measurement of the energy gap of the Landau levels as a function of the electric field strength and the tilt angle θ. Such measurements have been done in quantum Hall systems using microwave absorption techniques.[19] The variation in the excitation energy gap between the ground and the first-excited states, Δ_1, as shown in Fig. 6, should be observable in similar experiments performed with topological insulators. For $\mathcal{E} \geq v_F B \sin(\theta)$, we propose measurement of conductance G of these films as a function of both the electric field $\mathcal{E}$ and the tilt angle θ. We predict that for small $\mathcal{E}$, the tunneling should show a faster suppression with increase θ from 0 to $\pi/2$. We note that for a θ suitably chosen between 0 and $\pi/2$, the conductance of these films can tuned via an electric field, as demonstrated in Fig. 7, leading to realization of electric field controlled switching in these materials. For the NMN and NBM junctions, which can be prepared by depositing ferromagnetic films on the surface of a topological insulator, we propose measurement of the tunneling conductance G as a function of m_0. For the geometry shown in the left panel of Fig. 2, we predict that depending on the magnetization M, G should demonstrate either a monotonically decreasing or an oscillatory behavior as a function of the junction width d. Another, probably more experimentally convenient, way to realize this effect would be to measure V_c of a junction of width d for several values of M and confirm that V_c varies linearly with M with a slope of $\hbar v_F/(2e)$, provided μ and d remain fixed. For the geometry depicted in the right panel of Fig. 2, one would, in addition, need to create a barrier by tuning the chemical potential of an intermediate thin region of the sample as done earlier for graphene.[14] Here we also propose measurement of G_1 as a function of V_0 (or equivalently χ) for several representative values of m_0 and a fixed V. We predict that the maxima of the tunneling conductance would shift from $\chi = n\pi$ to $\chi = (n+1/2)\pi$ beyond a critical m_0 for a fixed V, or equivalently, below a critical V, for a fixed m_0. Finally, for the NMS junction, we propose measurement of the tunneling conductance $G(V)$ as a function of the magnetization M which should demonstrate the decaying behavior shown in Fig. 14. The tunability of the zero-bias conductance maxima, shown in Fig. 15, can also be tested by making junctions with different widths.

In conclusion, we have studied several magnetotransport properties of Dirac fermions on the surface of a topological insulator and have shown that they exhibit several properties which are distinct both from their counterparts in graphene and conventional Schrödinger electrons in other 2D systems. These novel features include tunability of the orbital and Zeeman effects of an applied magnetic field with a crossed in-plane electric field, realization of a magnetic switch using a NMN junction, and magnetic tunability of transmission resonances of Dirac fermions in NBM and NMS junctions. We have suggested experiments which can verify our theory.

ACKNOWLEDGMENTS

D.S. thanks DST, India for financial support under Project No. SR/S2/CMP-27/2006 and A. DaSilva for useful comments. K.S. thanks DST, India for financial support under Project No. SR/S2/CMP-001/2009 and K. Ray for several illuminating discussions on related topics.

[1] B. A. Bernevig, T. L. Hughes, and S.-C. Zhang, Science **314**, 1757 (2006); B. A. Bernevig and S.-C. Zhang, Phys. Rev. Lett. **96**, 106802 (2006).

[2] M. König, S. Wiedmann, C. Brüne, A. Roth, H. Buhmann, L. W. Molenkamp, X.-L. Qi, and S.-C. Zhang, Science **318**, 766 (2007); D. Hsieh, D. Qian, L. Wray, Y. Xia, Y. S. Hor, R. J. Cava, and M. Z. Hasan, Nature (London) **452**, 970 (2008).

[3] C. L. Kane and E. J. Mele, Phys. Rev. Lett. **95**, 226801 (2005); **95**, 146802 (2005).

[4] L. Fu, C. L. Kane, and E. J. Mele, Phys. Rev. Lett. **98**, 106803 (2007); R. Roy, Phys. Rev. B **79**, 195322 (2009); J. E. Moore and L. Balents, *ibid.* **75**, 121306(R) (2007).

[5] X. L. Qi, T. L. Hughes, and S. C. Zhang, Phys. Rev. B **78**, 195424 (2008).

[6] H. Zhang, C.-X. Liu, X.-L. Qi, X. Dai, Z. Fang, and S.-C. Zhang, Nat. Phys. **5**, 438 (2009).

[7] Y. Xia, D. Qian, D. Hsieh, L. Wray, A. Pal, H. Lin, A. Bansil, D. Grauer, Y. S. Hor, R. J. Cava, and M. Z. Hasan, Nat. Phys. **5**, 398 (2009); Y. Xia, D. Qian, D. Hsieh, R. Shankar, H. Lin, A. Bansil, A. Fedorov, D. Grauer, Y. Hor, R. Cava, and M. Hasan, arXiv:0907.3089 (unpublished).

[8] Y. L. Chen, J. G. Analytis, J.-H. Chu, Z. K. Liu, S.-K. Mo, X. L. Qi, H. J. Zhang, D. H. Lu, X. Dai, Z. Fang, S. C. Zhang, I. R. Fisher, Z. Hussain, and Z.-X. Shen, Science **325**, 178 (2009); T. Zhang, P. Cheng, X. Chen, J. Jia, X. Ma, K. He, L. Wang, H. Zhang, X. Dai, Z. Fang, X. Xie, and Q. Xue, arXiv:0908.4136 (unpublished).

[9] D. Hsieh, Y. Xia, D. Qian, L. Wray, J. H. Dil, F. Meier, J. Osterwalder, L. Patthey, J. G. Checkelsky, N. P. Ong, A. V. Fedorov, H. Lin, A. Bansil, D. Grauer, Y. S. Hor, R. J. Cava, and M. Z. Hasan, Nature (London) **460**, 1101 (2009); P. Roushan, J. Seo, C. V. Parker, Y. S. Hor, D. Hsieh, D. Qian, A. Richardella, M. Z. Hasan, R. J. Cava, and A. Yazdani, *ibid.* **460**, 1106 (2009); D. Hsieh, Y. Xia, L. Wray, D. Qian, A. Pal, J. H. Dil, J. Osterwalder, F. Meier, G. Bihlmayer, C. L. Kane, Y. S. Hor, R. J. Cava, and M. Z. Hasan, Science **323**, 919 (2009).

[10] L. Fu and C. L. Kane, Phys. Rev. Lett. **100**, 096407 (2008).

[11] A. R. Akhmerov, J. Nilsson, and C. W. J. Beenakker, Phys. Rev. Lett. **102**, 216404 (2009); Y. Tanaka, T. Yokoyama, and N. Nagaosa, *ibid.* **103**, 107002 (2009).

[12] T. Yokoyama, Y. Tanaka, and N. Nagaosa, Phys. Rev. B **81**, 121401(R) (2010).

[13] S. Mondal, D. Sen, K. Sengupta, and R. Shankar, Phys. Rev. Lett. **104**, 046403 (2010).

[14] A. H. Castro Neto, F. Guinea, N. M. R. Peres, K. S. Novoselov, and A. K. Geim, Rev. Mod. Phys. **81**, 109 (2009); C. W. J. Beenakker, *ibid.* **80**, 1337 (2008).

[15] M. I. Katsnelson, K. S. Novoselov, and A. K. Geim, Nat. Phys. **2**, 620 (2006); C. W. J. Beenakker, Phys. Rev. Lett. **97**, 067007 (2006); S. Bhattacharjee and K. Sengupta, *ibid.* **97**, 217001 (2006).

[16] Analogous situations may arise for graphene electrons in the presence of suitable gate voltages but not ferromagnetic films. See M. M. Fogler, F. Guinea, and M. I. Katsnelson, Phys. Rev. Lett. **101**, 226804 (2008).

[17] The orbital effect of a magnetic field along z in a multiple-barrier geometry may also reduce transmission in single and bilayer graphene. However, this property does not rely on the Dirac nature of graphene electrons. See M. R. Masir, P. Vasilopoulos, and F. M. Peeters, Appl. Phys. Lett. **93**, 242103 (2008).

[18] V. Lukose, R. Shankar, and G. Baskaran, Phys. Rev. Lett. **98**, 116802 (2007).

[19] A. Pinczuk, B. S. Dennis, L. N. Pfeiffer, and K. West, Phys. Rev. Lett. **70**, 3983 (1993).

[20] A. Shytov, N. Gu, and L. Levitov, arXiv:0708.3081 (unpublished); A. V. Shytov, M. S. Rudner, and L. S. Levitov, Phys. Rev. Lett. **101**, 156804 (2008).

[21] C. Xu, Phys. Rev. B **81**, 054403 (2010).

[22] S. Bhattacharjee, M. Maiti, and K. Sengupta, Phys. Rev. B **76**, 184514 (2007).

[23] M. König, H. Buhmann, L. W. Molenkamp, T. Hughes, C.-X. Liu, X.-L. Qi, and S.-C. Zhang, J. Phys. Soc. Jpn. **77**, 031007 (2008); G. Tkachov and E. M. Hankiewicz, Phys. Rev. Lett. **104**, 166803 (2010).